

RESEARCH ARTICLE

CHEMISTRY

Conjugated phthalocyanine-based framework as artificial SEI for over 400 Wh kg⁻¹ lithium metal battery

Ying Zang¹, Peng Peng³, Fei Pei^{2*}, Run-Han Li¹, Lin Wu², Di-Qiu Lu¹, Yi Zhang², Kai Huang², Yue Shen², Yun-Hui Huang^{2,*} and Ya-Qian Lan^{1,*}

¹School of Chemistry, South China Normal University, Guangzhou, 510006, China.

²State Key Laboratory of Materials Processing and Die & Mould Technology, School of Materials Science and Engineering, Huazhong University of Science and Technology, Wuhan 430074, China

³Henan Key Laboratory of Crystalline Molecular Functional Materials, Henan International Joint Laboratory of Tumor Theranostical Cluster Materials, Green Catalysis Center, College of Chemistry, Zhengzhou University, Zhengzhou, 450001, China

***Corresponding authors.** E-mails: peifei@hust.edu.cn; huangyh@hust.edu.cn;

yqlan@m.scnu.edu.cn

ABSTRACT

High-voltage lithium metal batteries (HVLMB) are appealing candidates for next-generation high-energy rechargeable batteries, but practical applications are still limited by the severe capacity degradation, attributed to the poor interfacial stability and compatibility between the electrode and electrolyte. In this work, a two-dimensional conjugated phthalocyanine framework containing single cobalt atoms (CoSAs-CPF) is developed as a novel artificial solid electrolyte interphase (SEI), where a large amount of charge is transferred to the CPF skeleton due to the Lewis acid activity of the Co metal sites and the strong electron-absorbing property of the cyano group (–CN), greatly enhancing the adsorption of Li⁺ and regulating Li⁺ distribution toward dendrite-free Li-metal batteries, superior to most of the reported

SEI membrane. As a result, the Li||Li symmetrical cell with CoSAs-CPF modified Li-anodes (CoSAs-CPF@Li) exhibits a low polarization with an area capacity of 1.0 mAh cm⁻² over 3500 h. The LiFePO₄||CoSAs-CPF@Li (LFP: 20 mg cm⁻²) delivers an ultra-long cycling life up to 1000 cycles with a high-capacity retention of 98.6%. Remarkably, the high-voltage LiNi_{0.8}Co_{0.1}Mn_{0.1}O₂||Li@CoSAs-CPF (NCM811: 10 mg cm⁻²) demonstrates a long cycling life over 800 cycles with a high-capacity retention of 80%. Meanwhile, in-situ ultrasonic transmission technology confirms the admirable ability of artificial CoSAs-CPF SEI to stabilize the Li-anode interface in pouch cells during cycling. Remarkably, the NCM811||Li@CoSAs-CPF pouch cell exhibits an energy density of 421 Wh kg⁻¹ and keeps 130 cycles with a low electrolyte/capacity ratio of 2.5 g Ah⁻¹. The strategy of constructing CoSAs-CPF-reinforced Li-anode provides a promising direction for high-energy-density HVLMB with long-cycling stability.

Keywords: conjugated phthalocyanine, artificial SEI, high energy density, lithium metal battery

INTRODUCTION

The development of portable electronic devices and electric vehicle technology has created a huge demand for high-energy-density energy storage systems. Lithium metal batteries (LMBs) have been accepted as one of the most appealing candidates to meet the increasing demand for the high-energy-density energy storage devices, due to the high theoretical capacity (3860 mAh g⁻¹) and low redox potential (3.04 V vs standard hydrogen electrode) of Li-metal anode [1–8], especially when coupling with high-voltage (LiNi_{0.8}Co_{0.1}Mn_{0.1}O₂ (NCM811)) and/or high-capacity (S and O₂) cathodes [5,9–11]. Unfortunately, the fast capacity degradation of LMBs and potential safety hazard, which are caused by the poor stability of solid electrolyte interphase (SEI) and uncontrolled Li-dendrite growth/pulverization, have limited further commercialization of the LMBs[2,4,12–15].

To solve these issues, multitudinous tactics have been exploited to reinforce the SEI layer by using various electrolyte additives or novel lithophilic current collectors [2,4,12,16,17]. Although these strategies have improved the uniform deposition of Li and cyclability of LMBs to some extent, in situ-generated non-uniform organic-inorganic hybrid SEIs are still insufficient to inhibit the growth of needlelike dendrites. In this case, artificial SEI film is considered as a highly effective way to solve interface problems of Li-anode due to (1) the chemical components of artificial SEI film are uniform, which is conducive to the uniform diffusion of Lithium metals; (2) it can be rationally designed to obtain a better morphological structure, and improve the electrochemical performance of the electrode interface and (3) it can effectively isolate the contact between electrolyte and electrode material, which reduces the electrolyte reaction, thus improving the coulomb efficiency [11,18–23]. It is worth noting that simultaneously fulfilling all the above requirements is challenging. In recent years, graphene films, Al_2O_3 , and lithium alloys have been widely used as a stable SEI film to isolate the unanticipated side reactions and protect Li anode, also have witnessed significant development for improving the interfacial stability of Lithium metal batteries [24–29]. Although some progress has been made, practical applications are still limited by how to achieve better chemical compatibility, more substantial Li ion transport efficiency, and more uniform lithium-ion deposition.

Conjugated phthalocyanine frameworks (CPFs) with unique structural flexibility [30–33], excellent flexibility/elasticity [34,35], and good physicochemical stability [35,36] show enormous potential for constructing artificial SEI: (1) The highly organic component composition exhibits excellent chemical compatibility/wettability with electrolyte; (2) The excellent flexibility and high elasticity guarantee the mechanical robustness of the SEI; (3) CPFs are functionally tailorable, which is conducive to the realization of a faster ionic conduction [20,37,38]; (4) the abundant functional coordination centers can uniformly provide metal sites with catalytic activity, thus in the conjugated skeletons with a high degree of uniform dispersion of single metal sites, the electron-rich state around metal atoms can optimize the Li^+ local coordination environment and promote Li^+ rapid migration, which is thought to

potentially have a good inducing effect on the homogeneous deposition of Lithium metals [38–41]. Notably, there is almost no two-dimensional fully π -conjugated conjugated CPFs that have been reported as artificial SEI layers to date.

Herein, we developed a pyrolysis-free route to synthesize a series of two-dimensional conjugated phthalocyanine frameworks containing different metal single atoms (MSAs-CPF, M = Fe, Cu, Ni, Co), the metal single atoms were stabilized effectively in the ultra-thin two-dimensional structure can guarantee higher atomic utilization, providing a more efficient charge transfer pathway. The mild synthetic route effectively reduces the agglomeration of MSAs-CPF and guarantees the utilization of the metal sites. More importantly, the Lewis acid activity of the MSAs sites and the strong electron-withdrawing property of the cyano groups promoted a large amount of charge transferred to the CPFs skeleton, which effectively enhanced the adsorption of Li^+ and suppressed Li dendrite. Meanwhile, MSAs-CPF-based flexible pack batteries also show longer operating life and higher capacity retention. By calculating, it is found that CoSAs-CPF shows a significant advantage in the adsorption and migration process of lithium ions, which keeps a high consistency with the subsequent experiments. A Li||Li symmetrical cell with CoSAs-CPF modified Li-anodes exhibited a low polarization with an area capacity of 1.0 mAh cm^{-2} for 3500 h. The CoSAs-CPF anode endows the high-loading LFP cathode (20 mg cm^{-2}) with a long cycling life up to 1000 cycles. Notably, the NCM811|CoSAs-CPF@Li cells can deliver a stable cycling life of 800 and 450 cycles with a loading of 10 mg cm^{-2} and 20 mg cm^{-2} , respectively. By using in situ ultrasonic imaging technology, the deterioration of the Li-anode interface in pouch cells during cycling can also be nondestructively shown. This is one of the pioneering systems to achieve a remarkable performance of HVLMB. The strategy of constructing CoSAs-CPF-reinforced Li-anode provides a promising direction for long-cycling life HVLMB.

RESULTS AND DISCUSSION

The conjugated quasi-phthalocyanine framework MSAs-CPF with single metal sites was synthesized by a solvothermal method according to our previous reports [30,31] (Fig. 1a). Then, the MSAs-CPF was dispersed in anhydrous DMF to form a uniform mixed solution of MSAs-CPF nanosheets (MSAs-NSs) after intense ultrasonic treatment. As shown in Fig. 1b, a facile roll pressing process was carried out to transfer MSAs-NSs onto the Li surface after the MSAs-NSs were filtrated on the polypropylene (PP) membrane, MSAs-NSs@Li was finally fabricated. The homogeneous nanosheet structure, good ionic conductivity, and uniformly distributed monatomic M active sites can regulate the uniform disposition of Li and endow a stable LiF-rich interface to effectively inhibit the growth of lithium dendrites and protect the Li anode.

To investigate the adsorption effect of Li on the different metal centers based conjugated quasi-phthalocyanine framework (Fig. 1a), the evaluation index of adsorption energy and migration energy barriers were obtained by charge decomposition analysis (CDA) and density functional theory (DFT) calculations. Differential charge density maps showed the electron density distribution between Li atoms and MSAs-CPF, and the charge limitedly accumulated in the skeleton, clearly indicating that the adsorption process is accompanied by Li–M–N charge transfer (Fig. S1). Subsequently, the adsorption energy of a Li atom adsorbing on the surfaces of MSAs-CPF is determined by DFT. As shown in Fig. 1c, all of the metal sites show a relatively strong adsorption energy effect toward Li, indicating that all these metals are lithophilic. Furthermore, the adsorption energies of Li^+ at peripheral cyanide sites were also conducted. As shown in Fig. 1c, the peripheral cyanide sites showed much higher adsorption energy, definitely indicating that Li^+ transferred at the peripheral cyanide sites was more difficult than that of metal sites. Thus, the Lewis acid metal sites in the polyphthalocyanine framework are ideal adsorption sites for lithium ions.

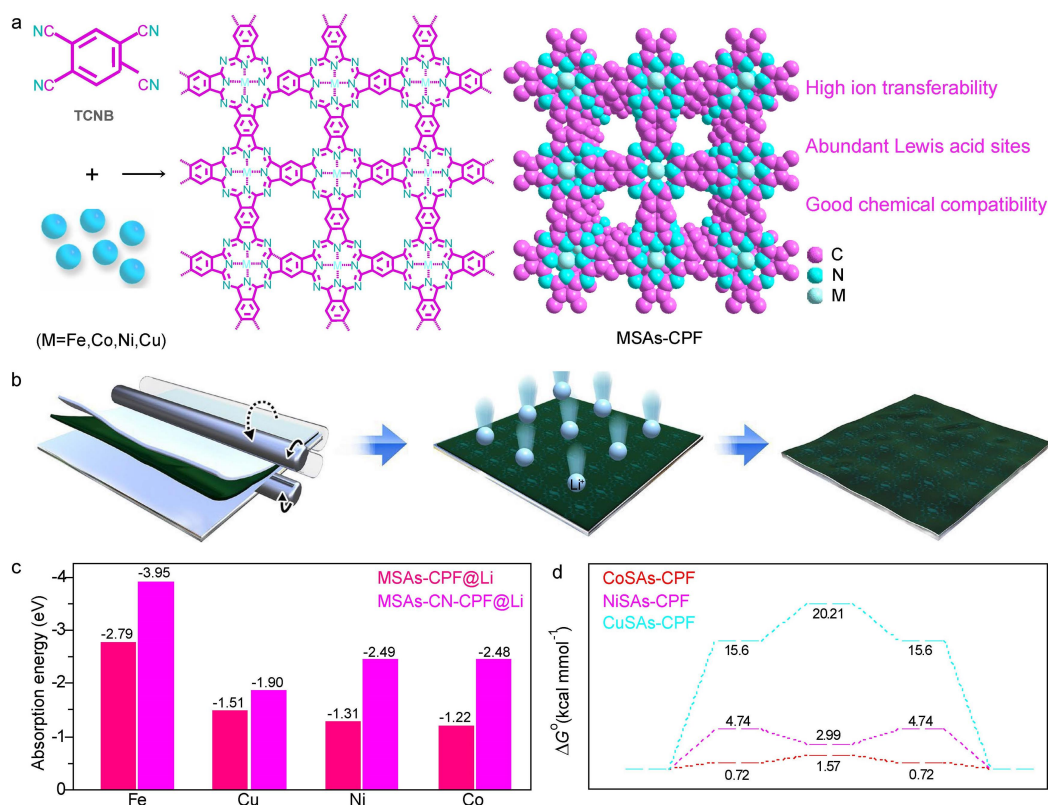


Figure. 1 | Structural design and comparison of lithiophilic properties of MSAs-CPF materials. (a) Schematic illustration of MSAs-CPF (M = Fe, Co, Ni, Cu). (b) Schematic illustration of the fabrication processes for MSAs-CPF@Li and Li deposition processes for MSAs-CPF@Li in lithium metal batteries. (c) Binding energy of Li atoms on MSAs-CPF and MSAs-CN-CPF. (d) The migration energy barriers of Li on CoSAs-CPF, NiSAs-CPF, and CuSAs-CPF.

A further analysis revealed that the CoSAs-CPF-based system presents relatively low adsorption energy of (-1.22 eV) with -2.79 eV of FeSAs-CPF, -1.51 eV of CuSAs-CPF, -1.31 eV of NiSAs-CPF, which suggests that the Li^+ has a strong binding ability on the surface of FeSAs-CPF and cannot complete the effective migration of Li^+ . While, CuSAs-CPF, NiSAs-CPF, and CoSAs-CPF adsorb Li^+ efficiently, and guarantee the migration process. In order to be more explicit, a calculation model based on monocyanothalocyanine instead of CPF was taken to illustrate the migration energy barriers of Li^+ on CuSAs-CPF, NiSAs-CPF and CoSAs-CPF surfaces through a series of structural Gibbs energy calculations (Fig. 1d and Figs S2–S4). By analyzing the migration potential energy surface of Li^+ , we could conclude that its migration is more likely to occur in the direction of M–N ring

→pyrrole ring→benzene ring. In addition, comparing the potential energy of Li^+ migration on the surface of Co (−1.22 eV), Ni (−1.31 eV), and Cu (−1.51 eV) centers, the energy to be overcome for Li^+ migration on the surface of Co centers was found to be relatively low (1.57 kcal/mol), which suggests that the surface migration of Li^+ is most thermodynamically favorable when the center metal is Co (Figs S5–S7). It is noteworthy that the polymerization of bis-phthalocyanine shows similar trends as monocyano-phthalocyanine, further proving that the outstanding Li^+ transport and performance in the CoSAs-CPF system could be ascribed to the Co sites. The above results indicate that MSAs-CPFs are ideal substrates for the adsorption of lithium. Benefiting from the effect of different Lewis acid metal sites, CoSAs-CPF is more favorable for the migration of lithium, so we synthesized CoSAs-CPF (NiSAs with a very similar results as a comparison), conducted the detailed structural characterization, and employed as the artificial SEI film of LMBs.

The characteristic peaks located at approximately 1547, 1697, 1711 and 1757 cm^{-1} in the Fourier transform infrared spectra (Fig. S8) represent that the specific macrocyclic structure of phthalocyanine was successfully constructed. In addition, the carbon structure of CoSAs-CPF was further confirmed by ^{13}C solid-state NMR (Fig. S9). The coordination environment of Co such as the valence state, coordination status and bonding configurations, were identified in depth by the X-ray photo-electron spectra (XPS) and the synchrotron-based XANES spectra (Fig. 2a–c). By comparison with those of the corresponding reference samples (Co foil, Co_2O_3 , Co_3O_4 , and cobalt phthalocyanine (CoPc), the Co K-edge XANES curves (Fig. 2b) showed that the pre-edge profiles of CoSAs-CPF are similar to that of CoPc, and only have a slight difference in intensities, indicating existence of the homogenous state of Co and the formation of Co–Nx coordination in CoSAs-CPF. As revealed by the extended X-ray absorption fine structure (EXAFS) spectra, the dominant peak generated by the Co–O (CoO as the reference) and Co–N species (CoPc as the reference) at ~ 1.62 Å demonstrated a similar absorption position with (CoPc) (Fig. 2c), implying the presence of N-coordinated single Co atom sites.

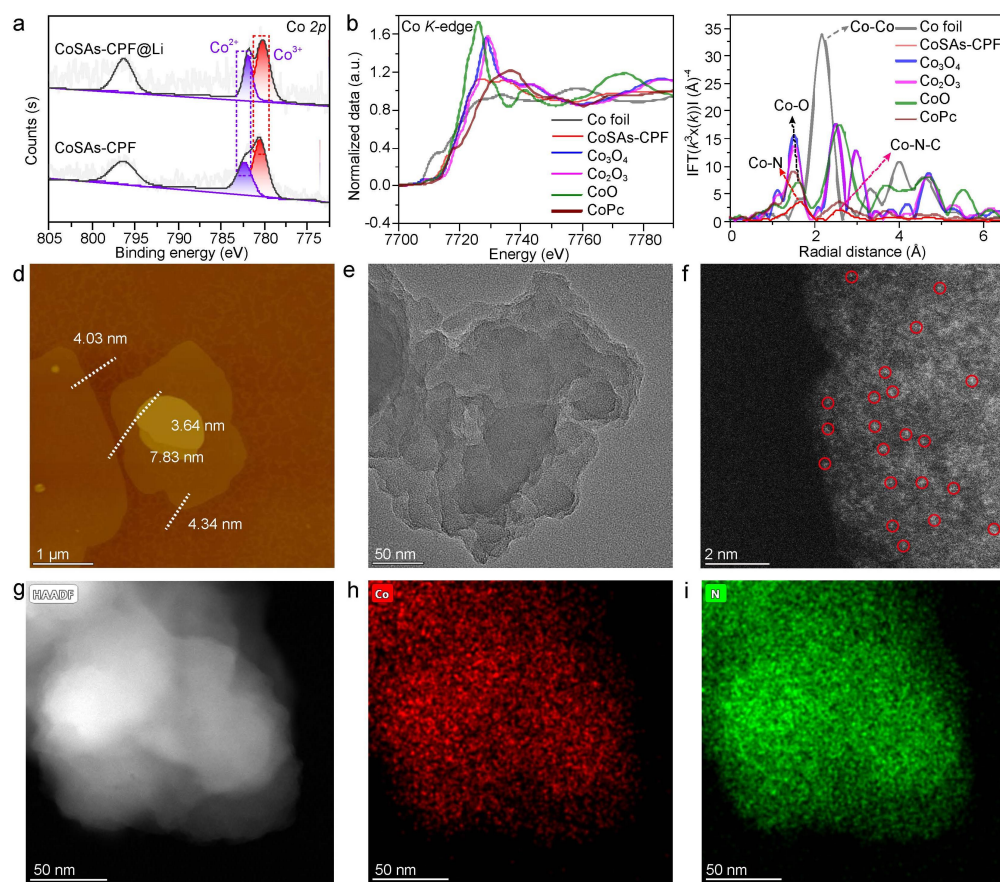


Figure 2 | Structural characterization of the CoSAs-CPF. (a) High-resolution Co 2p spectra of CoSAs-CPF, the black curves are the fitted data while the gray lines are the experimental results. (b) Normalized XANES and radial structure functions (RSFs) (c) of the Co K-edge obtained by Fourier transformation k3-weighted EXAFS results, with the Co foil, Co_2O_3 , Co_3O_4 and CoPc serving as references. (d) AFM image of CoSAs-CPF. (e) TEM image of CoSAs-CPF. (f-i) HAADF STEM image (f, g) and EDS-mapping (h, i) results of CoSAs-CPF.

Moreover, the absence of a peak at 2.17 Å belonging to the Co–Co metallic bond in CoSAs-CPF further validates the atomic dispersion of the Co atoms (Fig. 2c). Meanwhile, the prominent scattering path signal $[\chi(k), \chi(R)]$ of Co–N bonding of CoSAs-CPF in the first coordination shell is located at [3.79, 1.25], while a subtle scattering path signal of Co–C in the second coordination shell is located at [4.41, 2.23], which can be found in the wavelet transform of $\chi(k)$ spectra (Fig. S10). Furthermore, the characteristic scattering path signal of Co–Co bonding in Cu foil located at [7.12, 2.14] was not observed in the CoSAs-CPF, indicating again the atomic dispersion of the Co atoms in CoSAs-CPF. Collectively, the coordinated environment of Co sites in CoSAs-CPF was well elucidated by the Co K-edge

XANES curves, the related analysis results in R spaces and the wavelet transform of $\chi(k)$ spectra, and the single-atomic states of Co atoms were also clearly proved.

Meanwhile, CoSAs-CPF showed a two-dimensional slice morphology with a homogeneous distribution of different elements from the atomic force microscope (AFM) (Fig. 2d), scanning electron microscope (SEM) (Fig. S11) and transmission electron microscope (TEM) images (Fig. 2e and Fig. S12). The thickness of CoSAs-CPF was collected by AFM, which was confirmed as around 3.5–8 nm (Fig. S13), corresponding to 10–18 atomic layers. Furthermore, as revealed by SEM and TEM images, it can be observed that there is no aggregation of metal particles on the surface of CoSAs-CPF, indicating that the Co species were uniformly distributed on the CoSAs-CPF as the size of an atomic scale. Subsequently, the atomic structure of CoSAs-CPF was further explored by the high-angle annular dark-field scanning transmission electron microscope (HAADF-STEM) (Fig. 2f–i). From the aberration-corrected HAADF-STEM images of CoSAs-CPF, it could be observed that there is also no trace of the presence of aggregated states (Fig. 2f). The elemental mapping also suggests that the coordinated Co atoms were completely atomically and highly uniformly distributed on the surface (Fig. 2g–i).

CoSAs-CPF@Li was fabricated by a facile roll pressing process (Fig. 1b). The optical photographs of CoSAs-CPF@PP (inset of Fig. S14) show that CoSAs-CPF were uniformly pumped onto the PP membrane and formed a dense film with dark green (nearly black). Subsequently, the CoSAs-CPF@PP surface containing CoSAs-CPF was rolled onto 100 μ m Li metal to form CoSAs-CPF@Li, resulting in an artificial CoSAs-CPF SEI. Afterward, CoSAs-CPF @Li was cut into small discs with a diameter of 16 mm for button cell assembly and testing (Figs S15, S16). It's worth noting that the contact angle of CoSAs-CPF@Li is significantly smaller than that of Li foil, which indicates that CoSAs-CPF has a better wettability to the electrolyte, and further indicates that the artificial CoSAs-CPF SEI membrane has a good chemical compatibility (Fig. S17). In addition, the X-ray photo-electron spectra of CoSAs-CPF@Li was measured, and suggested a good stability to Li (Fig. 2a and Figs S18, S19). To further explore the induced behavior of different Lewis' acid sites

for Li deposition, NiSAs with isostructural were synthesized and NiSAs-NSs@Li was prepared by the same method. Afterward, detailed electrochemical tests were executed to evaluate its potential for practical application in lithium metal batteries.

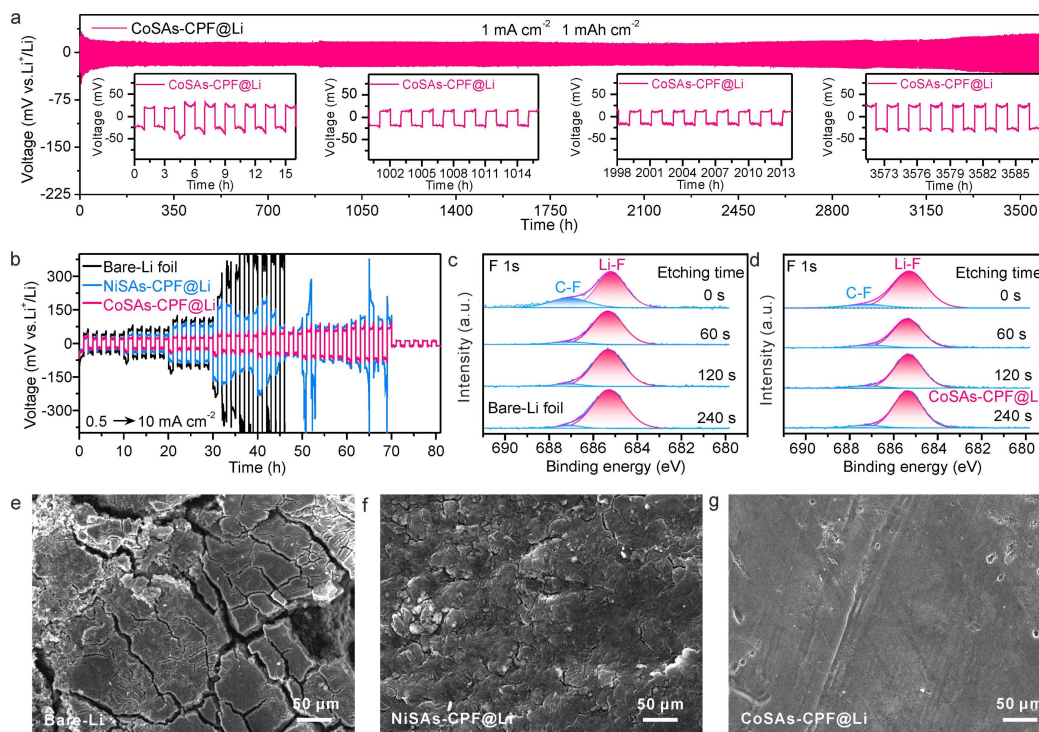


Figure 3 | Electrochemical stability of the Li||Li symmetric cells. (a) Galvanostatic cycling profiles of CoSAs-CPF modified Li||Li symmetric batteries with a current density of 1.0 mA cm⁻² and areal capacity of 1.0 mAh cm⁻². (b) Rate capabilities from 0.5 to 10 mA cm⁻² of Li||Li symmetric batteries with CoSAs-CPF@Li, NiSAs-CPF@Li and bare Li. (c, d) Depth-profiled XPS data for the cycled bare-Li anodes (c) and CoSAs-CPF@Li (d). (e-g) Top-view SEM images of the cycled bare-Li (e), NiSAs-CPF@Li (f), and CoSAs-CPF@Li (g) after rate cycles.

The constant current charging/discharging of Li||Li symmetric batteries were carried out to evaluate the effect of artificial CoSAs-CPF SEI on the Li deposition behavior and the cycling stability. As expected, under the constant current density of 1.0 mA cm⁻² and areal capacity of 1.0 mAh cm⁻² (Fig. 3a), the galvanostatic cycling profiles of symmetric batteries with artificial CoSAs-CPF SEI exhibit a prominent cycling stability for 3500 h and a low voltage fluctuation of ~40 mV. Meanwhile, the rate capabilities from 0.5 to 10 mA cm⁻² of CoSAs-CPF@Li, NiSAs-CPF@Li, and bare Li symmetric batteries were further tested with an area capacity from 0.5 to 10 mAh cm⁻² (Fig. 3b). It can be clearly that the voltage polarization increases as the current density increases, and CoSAs-CPF@Li showed the slightest voltage

polarization at different current densities, further highlighting its superior rate performance, and promoting the homogeneous deposition of Li. The X-ray photoelectron spectrum (XPS) of the cycled Li-anodes with different times of etching (0, 60, 120, and 240 s) were performed to further analyze the chemical composition of the newly formed SEI. As we all know, the inorganic LiF improves the uniformity of Li deposition and facilitates the stability of SEI, while the opposite is true for the inorganic phase C–F. As shown in the fitting consequences of Fig. 3c and d, the cycled CoSAs-CPF@Li showed significantly higher Li–F content and lower C–F content than that of cycled bare Li-anode, the inorganic Li–F are uniformly distributed at each etching depth, suggesting that the stable artificial CoSAs-CPF SEI causes the TFSI[−] anion to decompose preferentially into LiF, whereas the lower Li–F peak for cycled bare Li-anode means only a small amount of TFSI[−] reduced. In other words, CoSAs-CPF@Li delivered the ability to inhibit the further decomposition of electrolytes and keep the interfacial stability. After the rate cycles, the surface of cycled NiSAs-CPF@Li, and bare Li showed a severe crack and uneven, which is caused by the uneven uniformity deposition of the Li⁺, and on the contrary, the surface of cycled CoSAs-CPF@Li remained relatively smooth, which was consistent with the rate performance (Fig. 3e–g).

LFP||CoSAs-CPF@Li batteries with a high LFP loading (20 and 30 mg cm^{−2}) were employed to explore the potential application and practical feasibility of artificial-SEI. As a result, the specific capacity of the CoSAs-modified batteries with a LFP loading of 20 mg cm^{−2} was as high as 144 mAh g^{−1} at 1 C with a Coulombic efficiency of 99% and remained with almost no capacity degradation (98.6% capacity retention) after an ultra-long-life of 1000 cycles (Fig. 4a). As a comparison, the bare-Li and Ni SAs modified Li-anodes showed a similar initial capacity, but the capacity sharply dropped after 200 and 280 cycles, respectively. This is undoubted that the uncontrollable growth of Li-dendrite of LFP||NiSAs-CPF@Li and LFP||bare-Li breaking out to different extent. It is also exciting to note that, when an ultra-high LFP loading of 30 mg cm^{−2} was executed, the LFP||CoSAs-CPF@Li battery system contributed a capacity of 133 mAh g^{−1}, and only showed a slight

capacity decay tendency after continuing 533 cycles (Fig. 4b). Then these batteries are disassembled and replaced with fresh CoSAs-CPF@Li to assemble fresh batteries, the restarted battery can still maintain a stable life to 850 cycles under the same conditions. Such excellent results under ultra-high LFP loadings are uncommon and have been superior to most reported (Supplementary Tables S1, S2). Further to reflect that the designed artificial SEI (CoSAs-CPF) can effectively induce the uniform deposition of Li, and inhibit the decomposition of electrolyte and the growth of Li-dendrites even under an ultra-high LFP loading.

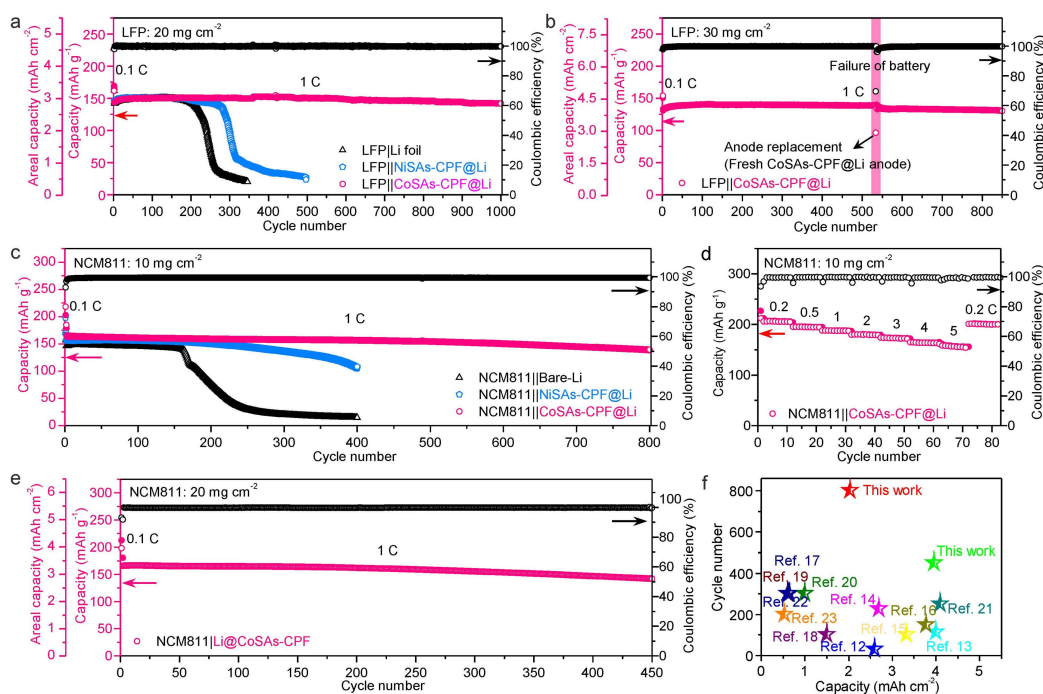


Figure 4 | Electrochemical performance of the LFP||Li and NCM811||Li batteries. (a) Cycling performance of LFP||CoSAs-CPF@Li, LFP||NiSAs-CPF@Li and LFP||bare-Li (20 mg cm^{-2}) at 1 C. **(b)** The cycling performance of LFP||CoSAs-CPF@Li (30 mg cm^{-2}) at 1 C. **(c)** Cycling performance of NCM811||CoSAs-CPF@Li, NCM811||NiSAs-CPF@Li and NCM811||bare-Li (10 mg cm^{-2}) at 1 C. **(d)** Rate performance of NCM811||CoSAs-CPF@Li (10 mg cm^{-2}). **(e)** Cycling performance of NCM811||CoSAs-CPF@Li (20 mg cm^{-2}) at 1 C. **(f)** Performance comparison of the coin-type batteries with the NCM811 cathodes.

We further investigated the practical potential of CoSAs-CPF@Li for high energy density cells of NCM811. The long-term cycling performance of NCM811||CoSAs-CPF@Li, NCM811||NiSAs-CPF@Li and NCM811||bare-Li (NCM811 loading: 10 mg cm^{-2}) was evaluated. As shown in Fig. 4c, after activation at 0.1 C for two cycles, NCM811||CoSAs-CPF@Li endows an initial capacity of 166

mAh g⁻¹ at 1 C, superior than that of NCM811||NiSAs-CPF@Li and NCM811||bare-Li (159 and 146 mAh g⁻¹, respectively). It is worth noting that NCM811||CoSAs-CPF@Li also contributed a prominent retention of up to 80% discharge capacity after long-time 800 cycles and a near-perfect coulombic efficiency (~ 99.4%), signifying the electrode materials were highly efficiently utilized and the efficiency of charging/discharging was guaranteed. Conversely, the NCM811||NiSAs-CPF@Li and NCM811||bare-Li possessed less than 80% capacity retention by 300 and 160 cycles, respectively. The discharge capacities of the NCM811||CoSAs-CPF@Li were 206, 196, 188, 180, 173, 164, and 157 mAh g⁻¹ at the current densities of 0.2, 0.5, 1, 2, 3, 4 and 5 C, respectively (Fig. 4d). Meanwhile, the capacity went back to the initial level with the rate switched back to 0.2 C. More importantly, by increasing the loading of NCM811 to 20 mg cm⁻² to meet the higher challenges in practical (Fig. 4e), after activation at 0.1 C for one cycle, NCM811||CoSAs-CPF@Li endowed an initial capacity of 166 mAh g⁻¹ at 1 C, achieved an outstanding stable cycling over 450 cycles at 1 C with 85.6% capacity retention, delivering a high Li⁺ utilization with a 99% coulombic efficiency. The performance is very competitive compared with other NCM811-based cathodes with modified Li anodes as shown in Fig. 4f, Tables S1 and S2 [42–53].

The digital photograph shows that the electrode size of the pouch cell is 6 cm × 8 cm (Fig. 5a). The cycling performance of the NCM811||CoSAs-CPF@Li pouch cell was investigated (Fig. 5b and c). The NCM811||CoSAs-CPF@Li cell with a high-loading cathode (NCM811: 20 mg cm⁻²) delivered a high discharge capacity of 210 mAh g⁻¹ (4.2 mAh cm⁻²) at 0.1 C. The discharge capacity in the first cycle of 0.5 C was as high as 190 mAh (198 mAh g⁻¹), and the pouch cell exhibited a discharge capacity of 169 mAh g⁻¹ after 140 cycles with 85.4% capacity retention. This provides a promising strategy for the design of high-energy-density and high-voltage lithium metal batteries. The ultrasonic imaging technique is an interface-sensitive method to test the wetting state and gas generation in pouch cell. The ultrasonic signal will be attenuated significantly in the vacuum or gas at the electrode interface than in

solids. The ultrasonic signal changes from red to blue, indicating that the signal strength changes from high to low.

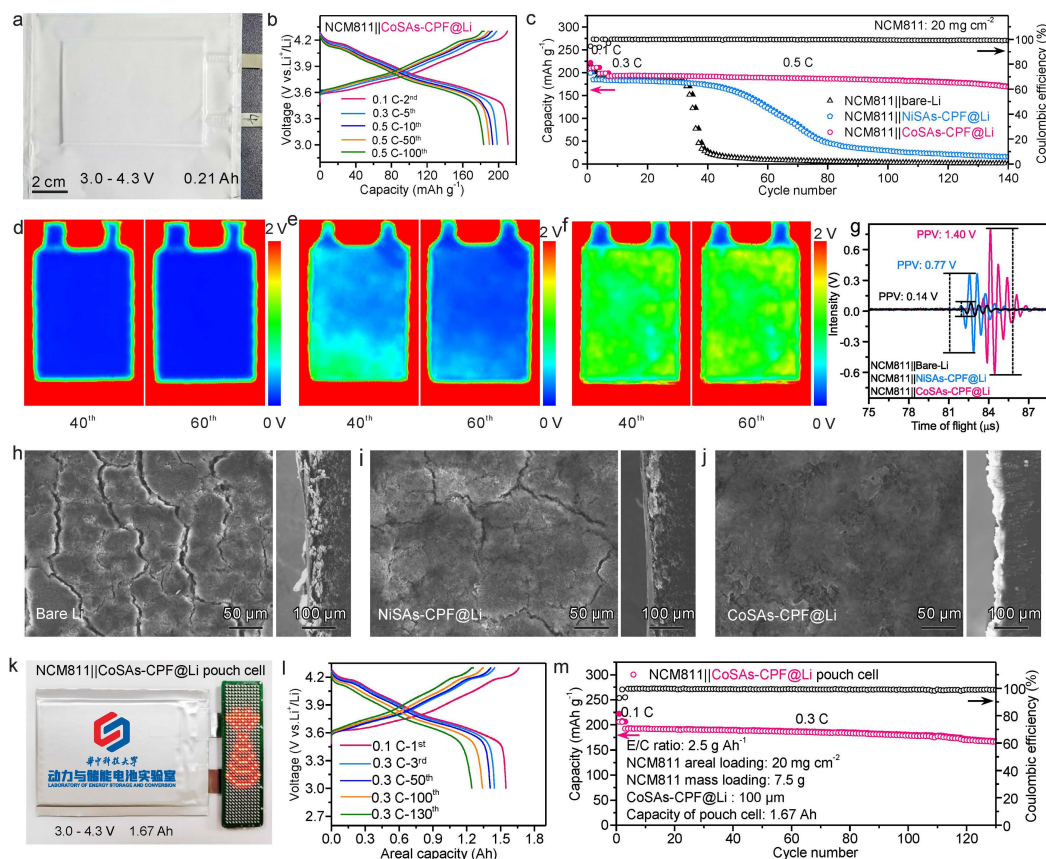


Figure 5 | Electrochemical properties of NCM811||Li pouch cells. (a–c) Optical images (a), charge/discharge curves (b), and cycling performance (c) of the NCM811||CoSAs-CPF@Li pouch cell. (d–f) In situ ultrasonic transmission images of NCM811||bare-Li (d), NCM811||NiSAs-CPF@Li (e) and NCM811||CoSAs-CPF@Li (f) during the first 60 cycles. (g) The comparison of corresponding representative ultrasonic voltage signal. (h–j) Top-view and cross-sectional SEM images of bare-Li (h), NiSAs-CPF@Li (i), and CoSAs-CPF@Li (j) after 60 cycles. (k) Optical image of NCM811||CoSAs-CPF@Li pouch cell lighting a LED lamp. (l, m) Charge/discharge curves (l) and cycling performance (m) of 1.67Ah NCM811||CoSAs-CPF@Li pouch cell.

The NCM811||bare-Li and NCM811||NiSAs-CPF@Li pouch cells showed inhomogeneity after cycling and the image gradually turned blue with the increased Li dendrite cycling number, explaining that the growth and severe pulverization of Li dendrites (Fig. 5d and e). However, the interface in NCM811||CoSAs-CPF@Li pouch remained in initial states with the cycle number increasing, indicating the existence of artificial SEI film stabilizes the lithium metal interface and prolongs the cycle life of the high-voltage battery (Fig. 5f). The corresponding representative ultrasonic signals

were shown in Fig. 5g, the average peak-peak amplitude values (PPVs) between the recorded maximum and minimum signals of NCM811||bare-Li, NCM811||NiSAs-CPF@Li and NCM811||CoSAs-CPF@Li after 60 cycles were 1.40, 0.77 and 0.14 V, respectively. The unstable interface of bare-Li metal caused the uncontrollable growth of lithium dendrites. The top-view SEM images of the cycles Li-anodes were collected by disassembling the NCM811||Li pouch cells after 60 cycles. Li dendrites on the cycled bare-Li foil and NiSAs-CPF@Li grew apparently. The surface of Li metal with NiSAs-CPF@Li appeared with many cracks and powders (Fig. 5h and i). As for the cycled CoSAs-CPF@Li appears to be relatively flat (Fig. 5j), the high mechanical strength of SPE and uniform Li^+ flux effectively suppressed the growth of lithium dendrites, creating a stable contact interface. More importantly, a high-capacity (1.67 Ah) multilayer pouch cell was assembled (Fig. 5k), further verifying the key role of protected Li-metal anode (CoSAs-CPF@Li) in extending cycle life. Under more demanding conditions, the electrolyte/capacity ratio (E/C) and the thickness of Li anode were set to 2.5 g Ah^{-1} and a total NCM811 loading of 7.5 g, the pouch cell exhibited a high charge capacity of 1.67 Ah at 0.1 C in the first cycle with a high initial Coulombic efficiency of 92.9%, after cycling steadily at 0.3 C for 130 cycles, a discharge capacity of 166 mAh g^{-1} were still kept with a high capacity retention of 86.5% (Fig. 5l and m).

CONCLUSION

In summary, a promising artificial solid electrolyte interphase (SEI) membrane was successfully explored and prepared using an atomically dispersed cobalt conjugated phthalocyanine framework CoSAs-CPF, to truly demonstrate the concept of the adsorption of Li^+ and effectively suppress Li-dendrite. The mild route of pyrolysis-free synthetic for CoSAs-CPF not only effectively reduced the formation of agglomeration, but also maintained the integrity of the structure, providing a new insight on preparing an artificial SEI with outstanding performance on stabilizing the traditional anode-electrolyte interface. Benefitting from highly atomically uniformly dispersed of cobalt Lewis' acid sites, excellent electron-withdrawal properties, good

charge-transferring ability, and stretchable flexibility, CoSAs-CPF modified SEI became an ideal platform for the construction of high-performance HVLMBs. As expected, the capacities, rate capabilities, and especially the cyclic stability of the batteries were significantly enhanced, superior to most of the reported SEI membrane. Given the diversity of CPF structures, chemically modifiable functional groups on organic linkers, and functional modulation of CPFs properties, it is believed that the concept of functionalized CPFs-based artificial SEI will push forward the future development of high-energy-density HVLMBs.

SUPPLEMENTARY DATA

The supplementary data are available at *NSR* online.

FUNDING

This work was supported by the National Key R&D Program of China (2023YFA1507204), the National Natural Science Foundation of China (22225109, 22201084 and 52202236) and China Postdoctoral Science Foundation (2022M711232, 2023M731155, 2023T160236 and 2024T170300).

AUTHOR CONTRIBUTIONS

Y.Q.L and Y.H.H. supervised and led this project. Y.Z. performed the synthesis and characterizations, F.P performed the electrochemical tests. Y.Z and F.P co-wrote this paper. R.H.L and Y.Z performed the theoretical calculation. Y.Z, R.H.L analyzed the theoretical calculation results. Y.Q.L., Y.H.H and F.P discussed the manuscript. All authors provided critical feedback, helped shape the research and manuscript, and commented on the manuscript.

Conflict of interest statement. None declared.

REFERENCES

1. Albertus P, Babinec S, Litzelman S *et al.* Status and challenges in enabling the lithium metal electrode for high-energy and low-cost rechargeable batteries. *Nat Energy* 2018; **3**: 16-21.
2. Liu B, Zhang JG, Xu W. Advancing lithium metal batteries. *Joule* 2018; **2**: 833-45.
3. Wang H S, Yu Z, Kong X *et al.* Liquid electrolyte: The nexus of practical lithium metal batteries. *Joule* 2022; **6**: 588-616.
4. Xiao J, Li QY, Bi YJ *et al.* Understanding and applying coulombic efficiency in lithium metal batteries. *Nat Energy* 2020; **5**: 561-68.
5. Jie YL, Liu XJ, Lei ZW *et al.* Enabling high-voltage lithium metal batteries by manipulating solvation structure in ester electrolyte. *Angew Chem Int Ed* 2020; **59**: 3505-10.
6. Shen X, Liu H, Cheng XB *et al.* Beyond lithium ion batteries: Higher energy density battery systems based on lithium metal anodes. *Energy Storage Mater* 2018; **12**: 161-75.
7. Lang JL, Qi LH, Luo YZ *et al.* High performance lithium metal anode: Progress and prospects. *Energy Storage Mater* 2017; **7**: 115-29.
8. Qin J, Pei F, Wang R *et al.* Sulfur vacancies and 1t phase-rich MoS₂ nanosheets as an artificial solid electrolyte interphase for 400 wh kg⁻¹ lithium metal batteries. *Adv Mater* 2024; **36**: 10.1002/adma.202312773.
9. Chen SR, Dai F, Cai M. Opportunities and challenges of high-energy lithium metal batteries for electric vehicle applications. *ACS Energy Lett* 2020; **5**: 3140-51.
10. Cheng XB, Zhang R, Zhao CZ *et al.* Toward safe lithium metal anode in rechargeable batteries: A review. *Chem Rev* 2017; **117**: 10403-73.
11. Wang XE, Kerr R, Chen FF *et al.* Toward high-energy-density lithium metal batteries: Opportunities and challenges for solid organic electrolytes. *Adv Mater* 2020; **32**: 1905219.
12. Meyerson ML, Papa PE, Heller A *et al.* Recent developments in dendrite-free lithium-metal deposition through tailoring of micro- and nanoscale artificial coatings. *Acs Nano* 2021; **15**: 29-46.
13. Rao XF, Lou YT, Zhong SW *et al.* Strategies for dendrite-free lithium metal anodes: A mini-review. *J Electroanal Chem* 2021; **897**: 115499.
14. Huo SD, Sheng L, Xue WD *et al.* Challenges of stable ion pathways in cathode electrode for all-solid-state lithium batteries: A review. *Adv Energy Mater* 2023; **13**: 202204343.
15. Pei F, Wu L, Zhang Y *et al.* Interfacial self-healing polymer electrolytes for long-cycle solid-state lithium-sulfur batteries. *Nat Commun* 2024; **15**: 351.
16. Wang JW, Wang KX, Xu YX, Emerging two-dimensional covalent and coordination polymers for stable lithium metal batteries: From liquid to solid. *Acs Nano* 2021; **15**: 19026-53.
17. Liu X, Mariani A, Adenusi H *et al.* Locally concentrated ionic liquid electrolytes for lithium-metal batteries. *Angew Chem Int Ed* 2023; **62**: e202219318.
18. Rosy, Naked M. Multifunctional interphase. *Nat Energy* 2018; **3**: 253-54.
19. Shi FF, Pei A, Boyle DT *et al.* Lithium metal stripping beneath the solid electrolyte interphase.

- Proc Natl Acad Sci USA* 2018; **115**: 8529-34.
20. Qiao Y, Zeng X, Wang H *et al.* Application and research progress of covalent organic frameworks for solid-state electrolytes in lithium metal batteries. *Materials* 2023; **16**: ma16062240.
 21. Liu W, Liu P, Mitlin D. Review of emerging concepts in SEI analysis and artificial SEI membranes for lithium, sodium, and potassium metal battery anodes. *Adv Energy Mater* 2020; **10**: 202002297.
 22. Zhang QK, Sun SY, Zhou MY *et al.* Reforming the uniformity of solid electrolyte interphase by nanoscale structure regulation for stable lithium metal batteries. *Angew Chem Int Ed* 2023; **62**: e202306889.
 23. Sun XW, Zhang XY, Ma QT *et al.* Revisiting the electroplating process for lithium-metal anodes for lithium-metal batteries. *Angew Chem Int Ed* 2020; **59**: 6665-74.
 24. Cheng DY, Wynn TA, Wang XF *et al.* Unveiling the stable nature of the solid electrolyte interphase between lithium metal and lipon via cryogenic electron microscopy. *Joule* 2020; **4**: 2484-500.
 25. Zeng J, Liu Q, Jia D *et al.* A polymer brush-based robust and flexible single-ion conducting artificial sei film for fast charging lithium metal batteries. *Energy Storage Mater* 2021; **41**: 697-702.
 26. Cao X, Jia H, Xu W *et al.* Review-localized high-concentration electrolytes for lithium batteries. *J Electrochem Soc* 2021; **168**: 010522.
 27. Chen MJ, Ma C, Ding ZP *et al.* Upgrading electrode/electrolyte interphases via polyamide-based quasi-solid electrolyte for long-life nickel-rich lithium metal batteries. *ACS Energy Lett* 2021; **6**: 1280-89.
 28. Tu HF, Li LG, Wang ZC *et al.* Tailoring electrolyte solvation for LiF-rich solid electrolyte interphase toward a stable Li anode. *ACS Nano* 2022; **16**: 16898-908.
 29. Westover AS, Sacci RL, Dudney N. Electroanalytical measurement of interphase formation at a Li metal-solid electrolyte interface. *ACS Energy Lett* 2020; **5**: 3860-67.
 30. Zang Y, Lu DQ, Wang K *et al.* A pyrolysis-free ni/fe bimetallic electrocatalyst for overall water splitting. *Nat Commun* 2023; **14**: 1792.
 31. Zang Y, Mi CX, Wang R *et al.* Pyrolysis-free synthesized catalyst towards acidic oxygen reduction by deprotonation. *Angew Chem Int Ed* 2021; **60**: 20865-71.
 32. Côté AP, Benin AI, Ockwig NW *et al.* Porous, crystalline, covalent organic frameworks. *Science* 2005; **310**: 1166-70.
 33. Ding S Y, Wang W. Covalent organic frameworks (COFs): From design to applications. *Chem Soc Rev* 2013; **42**: 548-68.
 34. Geng KY, He T, Liu RY *et al.* Covalent organic frameworks: Design, synthesis, and functions. *Chem Rev* 2020; **120**: 8814-933.
 35. Huang N, Wang P, Jiang DL. Covalent organic frameworks: A materials platform for structural and functional designs. *Nat Rev Mater* 2016; **1**: 16068.
 36. Zang Y, Wang R, Shao PP *et al.* Prefabricated covalent organic framework nanosheets with double vacancies: Anchoring Cu for highly efficient photocatalytic H₂ evolution. *J Mater Chem A* 2020; **8**: 25094-100.
 37. Lin Z, Wang Y, Li Y *et al.* Regulating solvation structure in gel polymer electrolytes with covalent organic frameworks for lithium metal batteries. *Energy Storage Mater* 2022; **53**: 917-26.
 38. Zhang K, Niu C, Yu C *et al.* Highly crystalline vinylene-linked covalent organic frameworks

- enhanced solid polycarbonate electrolyte for dendrite-free solid lithium metal batteries. *Nano Res* 2022; **15**: 8083-90.
39. Wang W, Yang Z, Zhang Y *et al.* Highly stable lithium metal anode enabled by lithiophilic and spatial-confined spherical-covalent organic framework. *Energy Storage Mater* 2022; **46**: 374-83.
 40. Xu Y, Zhou Y, Li T *et al.* Multifunctional covalent organic frameworks for high capacity and dendrite-free lithium metal batteries. *Energy Storage Mater* 2020; **25**: 334-41.
 41. Zhang C, Yang Y, Sun Y *et al.* 2D sp²-carbon-linked covalent organic frameworks as artificial SEI film for dendrite-free lithium metal batteries. *Sci China Mater* 2023; **66**: 2591-600.
 42. Han B, Xu D, Chi SS *et al.* 500 wh kg⁻¹ class Li metal battery enabled by a self-organized core-shell composite anode. *Adv Mater* 2020; **32**: 2004793.
 43. Shen Z, Zhang W, Li S *et al.* Tuning the interfacial electronic conductivity by artificial electron tunneling barriers for practical lithium metal batteries. *Nano Lett* 2020; **20**: 6606-13.
 44. Wu C, Guo F, Zhuang L *et al.* Mesoporous silica reinforced hybrid polymer artificial layer for high-energy and long-cycling lithium metal batteries. *ACS Energy Lett* 2020; **5**: 1644-52.
 45. Lee YH, Seo JY, Lee CD *et al.* Enabling sustainable lithium metal electrodes via cholesteric liquid crystalline cellulose nanocrystal nanomembranes. *Adv Energy Mater* 2022; **12**.
 46. Zhao Q, Utomo NW, Kocen AL *et al.* Upgrading carbonate electrolytes for ultra-stable practical lithium metal batteries. *Angew Chem Int Ed* 2022; **61**: e202116214.
 47. Zhu M, Fan Z, Xu K *et al.* An oxygen-resistant and self-eliminating passivated layer for highly stable lithium metal batteries. *Adv Funct Mater* 2022; **32**: 2112645.
 48. Zhao Y, Zhou T, Baster D *et al.* Targeted functionalization of cyclic ether solvents for controlled reactivity in high-voltage lithium metal batteries. *ACS Energy Lett* 2023; **8**: 3180-87.
 49. Chang C, Yao Y, Li R *et al.* Self-healing single-ion-conductive artificial polymeric solid electrolyte interphases for stable lithium metal anodes. *Nano Energy* 2022; **93**: 106871.
 50. Wang Z, Chen C, Wang D *et al.* Stabilizing interfaces in high-temperature ncm811-Li batteries via tuning terminal alkyl chains of ether solvents. *Angew Chem Int Ed* 2023; **62**: e202303950.
 51. Kim MS, Deepika, Lee SH *et al.* Enabling reversible redox reactions in electrochemical cells using protected LiAl intermetallics as lithium metal anodes. *Sci Adv* 2019; **5**: aax5587.
 52. Liu Q, Sun Y, Wang S *et al.* Highly adaptable SEI/CEI interfacial layers enabling remarkable performance of high-nickel solid-state batteries. *Mater Today* 2023; **64**: 21-30.
 53. Zhang C, Xie J, Zhao C *et al.* Regulating the lithium ions' local coordination environment through designing a cof with single atomic co site to achieve dendrite-free lithium-metal batteries. *Adv Mater* 2023; **35**: e2304511.